Numerical Investigation of Leading-Edge Tubercles on Aft Elements

Hamza Hussain[1]

[1] *Department of Mechanical and Aerospace Engineering, Brunel University Of London, United Kingdom*
[*] *hamza78624@icloud.com*

Compiled April 20, 2025

This report investigates whether leading-edge tubercles on an aft element on a multi-element aerofoil can enhance aerodynamic performance. Motivated by rising global aircraft fuel demands and the limitations of existing flow-control solutions, the current work aims to determine whether tubercles retain the flow benefits (that are previously reported on single-element aerofoils) when immersed in the fore element's wake. Using CFD and the k–ω SST turbulence model, simulations were conducted at a range of angles of attack with validation checks against historical NACA 23012 data. Analysis of surface shear stress, iso-surface plots and streamline contours revealed coherent streamwise vortex structures in the trough regions of the modified flap. Compared to a baseline configuration, the tubercled flap exhibited a 23 % increase in $C_{L,\mathbf{max}}$ and a 12.5 % increase in stall angle, achieving a more gradual loss of lift. Vortex core growth rate was found to be 0.00045 m α^{-1}, showing partial agreement with past studies. However, a steeper pitching-moment gradient was noted, indicating increased sensitivity to angle change. Overall, the study shows that a wavy aft leading edge (WALE) can improve aerodynamic performance in two-element aerofoils.

http://dx.doi.org/10.1364/ao.XX.XXXXXX

1. INTRODUCTION

Much of the existing research on leading-edge tubercles (LET) centre on their ability to reduce flow separation and delay stall when applied to single-element aerofoils. Although a number of studies confirm this and that tubercles can produce coherent streamwise vortices, most work has overlooked the more complex flow environment presented by multi-element, high-lift systems. In a typical two-element configuration, the fore element's wake interacts with the flap, modifying the local flow field in ways that may either reinforce or suppress the vortex structures created by tubercles. Exploring whether these tubercles can still operate effectively on a flap's leading edge is essential such that a successful outcome may introduce a new passive flow-control technique for boosting take-off and landing performance. By applying tubercles to the flap, engineers potentially gain an additional avenue for delaying stall and increasing overall lift, thereby reducing take-off speeds or runway length requirements. However, this feasibility is not guaranteed; the complex flow from the main element alone at higher angles of attack could diminish any advantage the tubercles might confer. Due to the fact that there is no significant published research which has examined tubercles on a flap's leading edge, the present project seeks to fill that gap by investigating their aerodynamic viability in a two-element system.

2. AIMS AND OBJECTIVES

The primary aim of this investigation is to understand whether tubercles introduced on a slotted flap's leading edge improve aerodynamic performance. This aim is deconstructed into two objectives:

(1) Identifying whether the flap tubercles still generate coherent streamwise vortices when immersed in the wake of the main element.

(2) Whether these generated vortices contribute to delaying stall and increasing the overall lift of the two-element aerofoil.

3. ACRONYMS

MTOW Maximum Take-Off Weight

ZFW Zero Fuel Weight

MEW Manufactured Empty Weight

VG Vortex Generator

PFC Passive Flow Control

RANS Reynolds-Averaged Navier–Stokes Equation

WALE Wavy Aft Leading Edge

T-S Tollmien–Schlichting wave

4. LITERATURE REVIEW

Before beginning any scientific investigation, it is customary to consider the underlying motives and potential future use of said investigation. In the context of an ever-growing global population and the attendant necessity for travel-impinging on nearly every working individual-one can deduce that the volume of civil aircraft traffic has inevitably increased, accompanied by a commensurate rise in fuel consumption; this will only increase with time. For instance, in 2019 the UK's annual aviation fuel demand was 12.3 million tonnes, projected to increase to approximately 17 million tonnes by 2050 [1]. This trend shouldn't be taken lightly. For the public to appreciate and grasp how aviation companies might accommodate larger fuel loads one day, it is in the best intentions to present such figures in the following qualitative way, thereby emphasising the wider implications to the public. Consider the following: any increase in an individual aircraft's fuel requirement calls for one of two options.

(1) The Maximum Take-off Weight (MTOW) could be increased to carry more fuel. As seen in Eq. (2), by relating Lift, L, to Weight, W, and rearranging for Velocity, V, it can be seen that the take-off velocity for an aircraft scales with $\sqrt{\text{MTOW}}$. When there arises a situation in which the velocity required for take-off increases, there are two things that can be done.

$$L = W = \frac{1}{2}\rho V^2 S_{\text{ref}}\, C_{L,\text{max}} \quad (1)$$

$$V = \sqrt{\frac{2W}{\rho S_{\text{ref}}\, C_{L,\text{max}}}} \quad (2)$$

The first is to increase the take-off distance such that the aircraft can reach the required velocity; the second is to improve propulsion technology so that engines provide necessary power. Yet propulsion developments are subject to extensive scrutiny, by (a) particular national aviation authority, and (b) protracted research-involving both wind tunnel testing and simulations-(a) and (b) must satisfy safety criteria. Any substantial increase in useful fuel results in allocating additional wing or fuselage space for it; there is a chance that this may potentially limit the volume available for passengers or cargo.

(2) If the MTOW is to remain unchanged, due to an increase in total fuel load, the Zero-fuel Weight (ZFW), which includes payloads, must decrease. This lowers the total cargo weight, passenger capacity, baggage allowance, or a confluent reduction across all three. Such reductions inevitably compromise customer satisfaction-particularly due to baggage restrictions or operators raising baggage fees. Similarly, curbing the total passenger weight may lead to fewer available seats or increased flight ticket costs, both of which adversely affect the commercial aspect of flight.

Having said that, reducing the Manufacturer's Empty Weight (MEW) in a way that will allow the weight of payload to remain unchanged is a viable method to mitigate the restrictions that were mentioned previously. This reduction can be achieved using materials such as thermoplastics. In a NASA presentation by Robert G. Bryant, he outlined the benefits of thermoplastics, including reduced weight and increased durability [2]. However, their current application is limited to smaller components like wing tips and window frames. The long-term goal is to extend their use to larger structures such as the fuselage and wing skins. For further details on the advantages, challenges, and manufacturing processes of thermoplastics, refer to [2]. After having read the aforementioned effects of rising fuel demands, it should be made clear to the reader that an approach be made to reduce fuel usage. This can be achieved via reducing the required velocity for known flight phases such as take-off/landing or cruise. Examining Eq. (2) further, to increase V, ρ, S_{ref} and $C_{L,\text{max}}$ must increase. The first two may be assumed constant, as increasing ρ is currently very difficult and increasing S_{ref} leads to an increase of parasitic drag scaled by S_{wet}. Thus the equation is rewritten in the following form:

$$V = \sqrt{\frac{2W}{\rho S_{\text{ref}}}}\sqrt{\frac{1}{C_{L,\text{max}}}} \quad (3)$$

By considering $\sqrt{\frac{2W}{\rho S_{\text{ref}}}}$ as a constant, A, Eq. (3) shows that velocity inversely scales with $\sqrt{C_{L,\text{max}}}$ such that if $C_{L,\text{max}}$ increases by 20 % at take-off, the required take-off velocity will decrease by 4.5 %. This relationship has been plotted, taking the value of A as some arbitrary value that is canonical to smaller aircraft. From Figure 1, if the lift increases by 40 %, this only results in a 13 % reduction in flight velocity. By reducing the take-off velocity, the runway length can also be shortened. The matter now lies in increasing $C_{L,\text{max}}$.

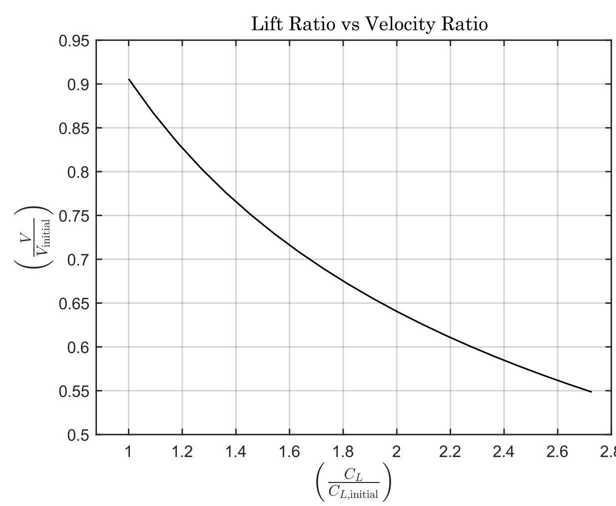

Fig. 1. Variation of velocity ratio against increase of lift ratio for a small aircraft.

$C_{L,\text{max}}$ is a dimensional parameter which represents the lift of a surface subject to moving air. It is the maximum lift a body can produce before encountering a sudden drop in lift nominally called stall which occurs due to flow separating into a laminar and circulating region. The methods used in increasing lift via virtual methods is under the heading Lift Augmentation and comes within the scope of this current investigation; however, before all it will be of great use to understand the concept of Turbulence, a brief definition of it, and the relevant forms of drag.

There are two types of flow, Laminar and Turbulent. Laminar flow has streamlines which follow a smooth path. Turbulent flow is considered more ’disordered’ than laminar flow, and the transition to turbulence is often seen as a natural inevitability, given that most aerodynamic problems involve turbulence. The perspective that turbulence equates to disorder is widely accepted across fundamental aerodynamic literature; however, equating turbulence solely to ’disorder’ warrants further scrutiny. The Cambridge Dictionary defines disorder as a “lack of organisation,” insinuating a gap in knowledge within this field. Another way of interpreting this definition is that there is insufficient chapterisation- since, as is often seen within academic spheres, the science of chapterisation and the segmentation of a field into various conditions and rulings facilitate the learning process of others. The Cambridge definition perhaps stems from the historical difficulty in understanding turbulence. In [3], Jiménez suggests that turbulence should be approached as a deterministic system rather than as inherently random, later arguing that to analyse coherent structures within turbulence, it may be more rigorous to consider the flow in a statistically averaged framework. A more accurate descriptor of turbulence is chaotic, as the term itself originates from chaos, making it reasonable to draw parallels with chaos theory, that is, if turbulent flow is understood as a Strange Attractor, then there lies a great deal of dependence and sensitivity on the initial conditions of the flow. Turbulent Strange Attractors exhibit chaotic flow within a closed boundary, Ω; however, the global nature of the flow can be considered statistically structured. The current understanding of turbulence can be deconstructed in terms of three key facets:

1. **Why turbulence occurs:** Turbulence arises from the instability of laminar flows under high Reynolds Numbers, Re, in which inertial forces take over the viscous forces which can no longer ‘smoothen’ the flow. Natural transition to turbulence is solely due to infinitesimal disturbances in the flow, which may develop to notable 2D disturbances, such as Tollmien–Schlichting waves [4]. The presence of T–S Waves lead to the escalation of turbulent spot bursts, eventually resulting in a homogenised turbulent region. The second form of transition is known as Bypass Transition. There are a number of different ways this can happen. One of them is that somewhere along the body lies a rough surface, which quite literally ‘trips’ the flow into each other; this is seen in Fig. 2.

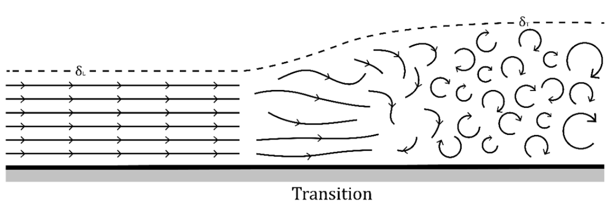

Fig. 2. Flow over flat plate undergoing bypass transition.

Bypass transition may also occur due to an adverse pressure gradient along the surface, this is due to a pressure recovery process by the ambient pressure unto the boundary layer, adverse pressure gradients are completely due to aerofoil geometry and how sharp their leading edge corners are. The presence of an adverse pressure region leads to the decelerating and reversal of fluid elements, a cascade of energy from larger to smaller scales, this energy cascade underpins the ‘chaotic’ appearance of turbulence.

2. **Modelling of turbulence:** Computational-Fluid-Dynamics (CFD) represents a significant advancement in engineering capabilities, allowing for fluid simulation that approximates real-world behaviour with a certain degree of accuracy. This contemporary approach substantially reduces both time and financial resources, which are required for innovation in systems dependent on fluid. This methodology begins with a continuous domain, discretised into a structured grid, transforming a physical space into a framework where flow variables can be calculated. At the intersection points of this grid lie nodes, which collectively form quadrilaterals or triangles, called cells. At each node flow variables are defined and solved through numerical methods. For simulations involving flow around complex geometries, the Finite-Volume method is implemented; this method has become an industry standard, used in commercial software packages such as FLUENT. Cells in the domain may be considered discrete control volumes (CVs) bounded by sides dS in which the integral form of the conservation equations is applied to each CV. The integral form of the continuity equation is given in Eq. (4):

$$\frac{\partial}{\partial t}\iiint_V \rho\, \mathrm{d}V + \iint_S \rho\, \mathbf{V}\cdot \mathrm{d}\mathbf{S} = 0 \tag{4}$$

Newton’s second law is applied to each CV as well in a Eulerian approach. It is known that there are three reasons why total momentum inside a CV may change.

(a) Momentum flux across dS, denoted by outer product of mass flux across dS by velocity term u, $\rho(u \otimes x)\cdot dS$.

(b) Forces acting upon dS, which are defined at each node as a Cauchy stress tensor, σ, passing through the normal. σ contains an isotropic stress (due to the presence of a pressure field) and a deviatoric stress which captures sheer and normal stresses; see Eq. (6) for the expanded formula for the Cauchy stress tensor.

$$\sigma = -pI + \sigma_d \tag{5}$$

$$\sigma = -pI + \{\mu(\nabla u + (\nabla u)^T) \pm \tfrac{2}{3}\,\mu(\nabla \cdot u)\, I\} \tag{6}$$

In Eq. (6), p represents pressure per unit area, I represents the identity matrix, and μ represents the dynamic viscosity.

(c) Any external force, b_f, acting upon dV, such as gravity.

By applying Newton’s second law and accounting for these causes of momentum change, the differential form of the momentum conservation formula is found, nominally known as the Navier–Stokes equation. See **??**

$$\frac{D}{Dt}\rho\, u + \rho\, u(\nabla\cdot u) = -\nabla p + \nabla\cdot\sigma_d + b_f \tag{7}$$

The work of this report does not exceed Mach 1, therefore temperature change and compressibility effects need not be discussed and the energy equation will not be discussed in conjecture. If flow was considered entirely laminar then Eq. (7) becomes straightforward to simulate, however it was made clear previously that turbulence is an effect that should always be considered in problems. To account for turbulence, Eq. (7) must be revised. By decomposing each instantaneous flow variable into a mean and fluctuating part (Reynolds decomposition).

$$\phi(x,t) = \bar{\phi}(x,t) + \phi'(x,t)$$

Applying this decomposition to every variable in the Navier–Stokes equations and then taking an ensemble average yields the Reynolds–Averaged–Navier–Stokes (RANS) equation and an extra term, the Reynolds Stresses-$\rho\ (u' \otimes u')$- which represents momentum exchange solely due to turbulence. Reynolds Stresses introduce new unknowns, leading to the so-called closure problem, to address this succinctly, turbulence models provide relationships between Reynolds Stresses and mean flow field. For a fuller treatment of CFD, see [5]

3. **Taming turbulence:** Controlling turbulence is challenging however respectable approaches have been made to do so. What is really meant by 'taming' turbulence is that turbulent flow is either induced such that drag is reduced or the transition to turbulence is delayed. This report pertains more to the latter, that is, delaying flow separation (which in low Reynold's number cases results in either reattachment, this is a separation bubble and more times than one, the flow that reattaches is turbulent.)

So the subject of the report expands upon the third facet. Managing turbulence effectively with the goal of lift augmentation means one should know when turbulence is desirable or undesirable and this relies on the prerequisite knowledge concerning the surface geometry and the type of drag it will experience, therefore, in conjunction, flow separation is a key design factor. This report assumes operation at subsonic speeds, thus excluding Wave Drag from consideration. The primary forms of Parasitic Drag relevant here are Form Drag and Skin Friction Drag.

(1) **Form Drag**, D_p, also known as Pressure Drag, this is due to flow separation, both steady and unsteady. Flow separation is one of the more critical aerodynamic phenomenon present in an aircraft that significantly impacts the aircrafts performance, especially near maximum lift conditions. It initiates with the presence of an adverse pressure gradient, where the pressure along the aerofoil chord increases in the direction of the flow, this region is normally aft of the aerofoil. In such regions, the greater downstream pressure exerts a force against the oncoming flow, causing it to decelerate, eventually reaching a point where $u = 0$, subsequently the flow reverses, creating a separation point. At the point of separation, airflow splits into two distinct regions: the laminar region above the inflection point, where the flow continues to remain smooth, and the wake region below it, where the flow circulates. Once separation occurs, the pressure distribution further aft of the separation point is notably reduced, creating a pressure imbalance, with higher pressure towards the rear of the aerofoil. The resulting imbalance substantially increases D_p leading to a significant drop in aerodynamic efficiency and potentially causing stall. This type of drag is closely tied to the body's geometry; Shapes with greater corner radius, where the flow travels more distance from the stagnation point to the end of the turn, tend to experience D_p due to the inability of the flow to restabilise itself. In an ordinary aerofoil the pressure must recover along the surface such that the pressure at the trailing edge equal to greater than the local pressure, or else it will risk separation.

(2) **Skin-friction drag**, D_f, is caused from the shear stress between adjacent fluid layers and the surface of the body due to viscosity. It is directly proportional to the velocity gradient in the boundary layer, with the constant of proportionality being the viscosity constant, μ, and is directly influenced by the total surface area exposed to the flow.

Turbulence is desired when D_p is more likely to dominate D_f, this is typically the case for bluff bodies such as cylinders or nacelles. Turbulent flow is far more resistant to separation than laminar flow, its larger boundary layer thickness (δ) promotes near-wall momentum fluxes, which help keep the flow attached for a longer distance. Regarding separation, passive flow control (PFC) structures like vortex generators (VG's) are frequently employed to energise the boundary layer and delay separation even further. VG's are small, fin-like devices mounted near the leading edge [6], or other critical areas prone to flow detachment, where they exploit local pressure differences to create swirling motions. These vortices inject additional kinetic energy into the boundary layer, producing a 'fuller' velocity profile that counters adverse pressure gradients and postpones separation. Fig. 3 illustrate this process: vortices generated by multiple VG's drive high-momentum air into low-momentum regions, reducing form drag by maintaining attached flow over a greater portion of the surface. Likewise, laminar flow is generally preferred when friction drag (D_f) outweighs pressure drag (D_P), because the near-wall velocity gradient and hence the shear stress remains notably lower under laminar conditions. However, introducing passive flow-control devices such as vortex generators simply increases the wetted surface area, thereby amplifying D_f and negating some of the advantages offered by a laminar boundary layer.

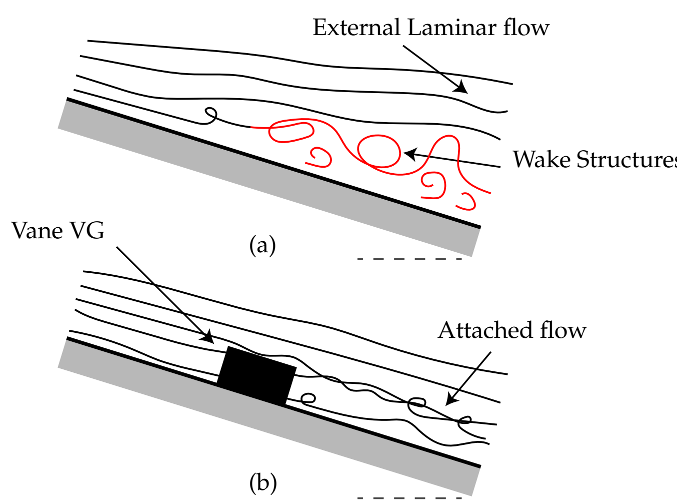

Fig. 3. Angled flow over (a) flat plate and (b) a Vane VG.

It is well known that the aero-requirements of an aircraft vary significantly between the different flight phases. During take-off and landing, flow separation is more likely to occur due to high angles of attack and subsequent adverse pressure gradients, making designs that mitigate D_p particularly valuable. Conversely, during cruise, where flow is predominantly laminar and the risk of separation is minimal, designs optimised

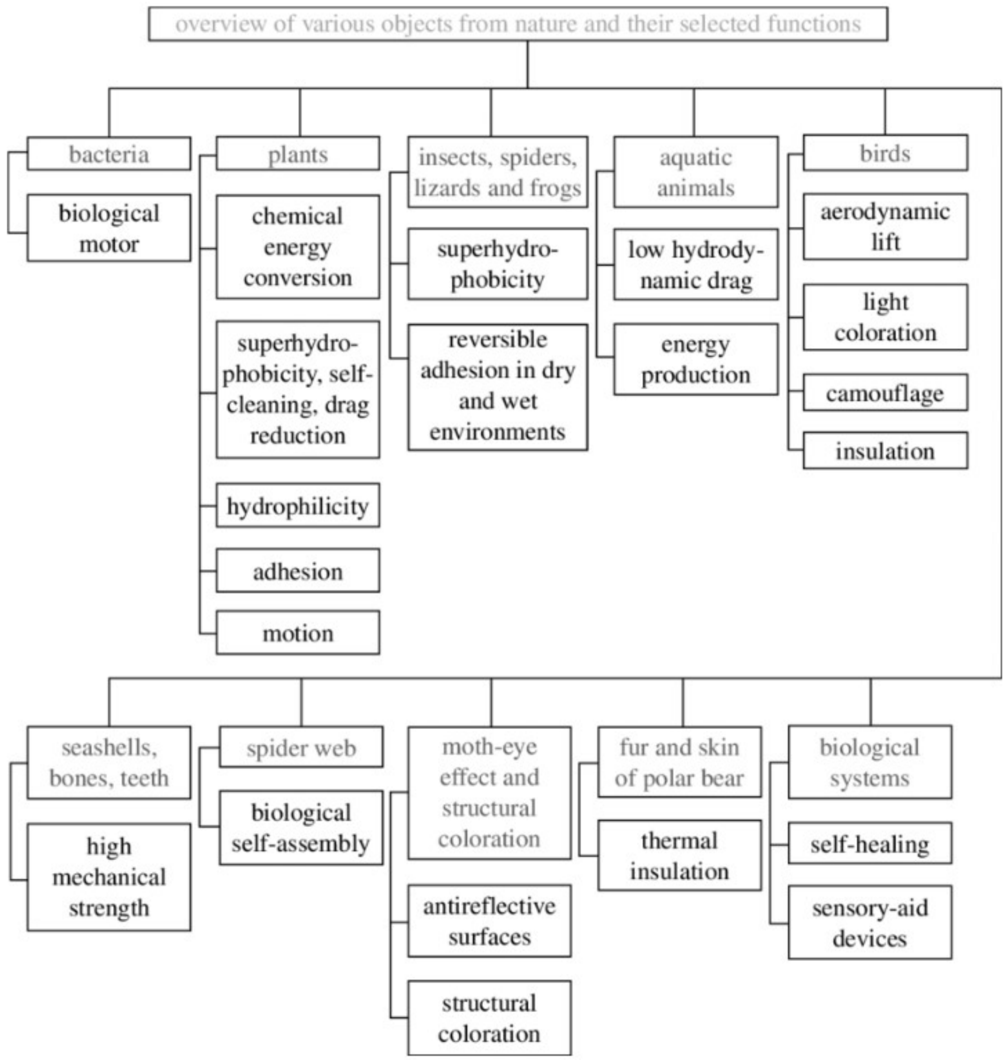

Fig. 4. '*An overview of various objects from nature and their selected functions.*' [7].

to minimise skin-friction drag D_f become more desirable. Vane vortex generators have traditionally been employed to delay the onset of flow-separation during take-off and landing but their fixed implementation increases surface friction, which becomes a drawback during cruise. Recognising this trade-off,Mustafa Özden et al [8] have explored deployable VG designs, hidden in flaps, allowing them to be activated when needed and retracted during cruise when not needed, see Fig. 5. These were found to contribute to a positive effect with increasing velocity. Similar patents have been filed which incorporate VG's that synchronously deploy with the flap [9][10][11].

Another PFC approach involves biomimicry-drawing on the evolutionary adaptations found in nature to improve man-made systems. Note, not all natural solutions are inherently an optimal solution (e.g. although the human foot is suited to bipedal locomotion, it is far less efficient, in terms of energy expenditure, than a kangaroo's foot, which stores and releases energy via elastic tendons). In aerospace, where increased performance is always in demand, numerous flow control devices-from aerofoil modifications (flaps, slats) to VG's-have emerged. Each carries trade-offs, so the quest for an integrated and holistic design continues. Bhushan [7] illustrates several nature-inspired innovations, as shown in Figure 4.

It has been recognised for some time that humpback whale dorsal fins feature prominent leading-edge protuberances, or tubercles. Fish and Battle [12] first noted these protuberances, describing their nodal spacing and proposing that these structures act in a similar way as vortex generators, contributing to the whale's manoeuvrability. Though Fish and Battle were the first to suggest the high lift properties of these whales, the notion that marine species are capable of drag reduction via longitudinal vortices is not new, and was reported more than 33 years before Fish and Battle [13]. For additional insight into how animals minimise drag, see [14].

Interestingly, there is evidence in the fossil records that similar structures appeared much earlier in evolutionary history. For instance, in the order *Iniopterygia*, which includes prehistoric fishes that show hook-shaped bumps along the leading edges of their elongated fins. This suggests a potential hydrodynamic function similar to that of modern tubercles found on hump-

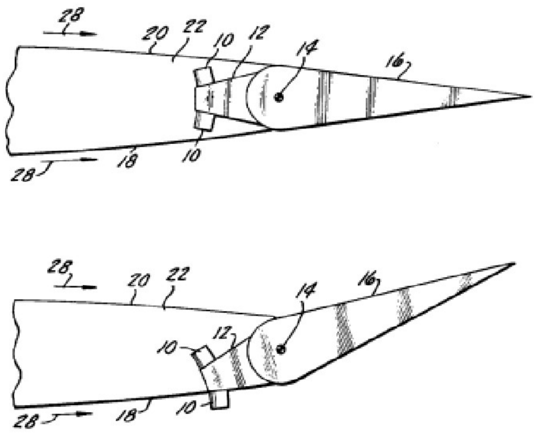

Fig. 5. Retractable Vortex Generator design ([9]).

back whales. Moreover, the genus *Protosphyraena*, a member of a group of swordfish- like predatory marine fishes from the Upper Cretaceous period- also displayed characteristics that may be analogous to tubercles, as shown in Figure 6.

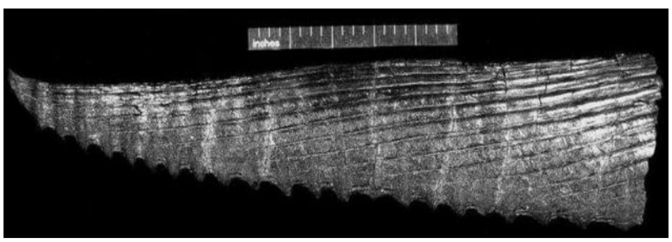

Fig. 6. Image of Protosphyraena pectoral fin by W. Buckley [15], leading edge serration can be seen.

Using 3D panel methods, Watts and Fish [16] studied a low-aspect-ratio wing equipped with leading edge tubercles (LET). They observed a 4.8% lift increase at 10° angle of attack, with minimal adverse effects as the angle approached 0°. However, the increase in D_f roughly balanced the induced drag savings at 10%, and the most significant performance gains were realised beyond 15%. Subsequent research featured wind tunnel experiments on machined, scaled flipper models with and without tubercles [17]). Their results indicated a 6% improvement in maximum lift and roughly a 40% delay in stall angle relative to the baseline configuration. Studies from Zhang et al [18] and Keerthi et al [19] help to corroborate the initial observations by Fish. Although promising, LET have their drawbacks, such as a drop in post-stall performance. Stein and Murray [20] observed a drop in lift and an increase in drag between 8° and 12° on a two-dimensional aerofoil with whale-scale tubercle amplitudes. This is confirmed by Joseph and Sathyabhama [21] noting that while tubercles excel in post-stall flight, they can produce unwanted drag and reduced lift in the pre- stall conditions. Introducing LET on slightly swept wings reported enhanced aerodynamic performance with increasing sweep angle [22].

A common misconception is that LET's function similarly to vane VG's; this comparison has been used by the majority of authors mentioned in this section. Although both devices share the common goal of delaying stall by maintaining attached flow, tubercles behave more like small leading edge delta wings (see Figure 7).

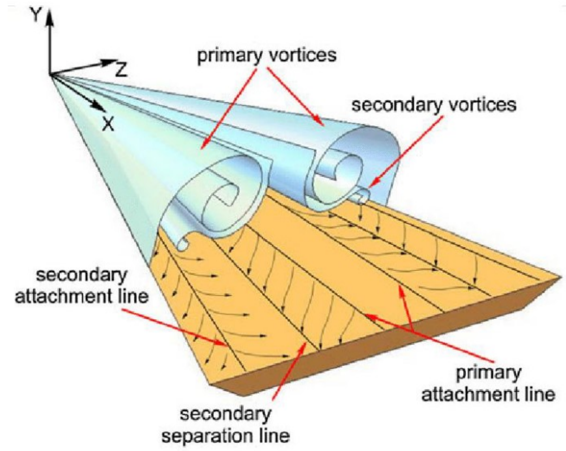

Fig. 7. Vortex Lift for a highly swept delta wing ([23])

Each tubercle "bump" forms a conically rolled vortex sheet from its curved apex, extending spanwise along the leading edge. Trapped by local airflow, this vortex adheres to the upper surface, reattaching in the trailing region. While tubercles and vane VG's share the general goal of enhancing lift by postponing flow separation, the underlying mechanisms differ. This must be made clear. In particular, isosurface vorticity plots [24] show that tubercles generate discrete, streamwise vortex structures that confine leading-edge separation to localised tip regions, thereby delaying full flow detachment, the vortices are seen in Figure 8.

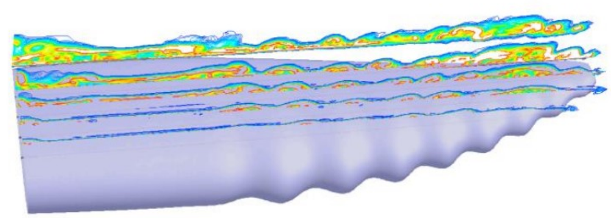

Fig. 8. Turbulent Intensity contour plot over humpback flipper ([24]).

The reader should understand that tubercles, on their own, are a PFC technique, they cannot be switched off at will with the goal of reducing S_{wet} during flight phases where high lift is not required (cruise). Having understood this, the reader may ask whether there have been attempts at producing Active Flow Control methods for LET. Two viable methods have been proposed in the literature.

1. **Plasma Actuators**: Studies performed [25]demonstrate that plasma actuators can be utilised to function as virtual tubercles. An increase of voltage supplied to the actuator relates to a virtual increase to the tubercle amplitude; likewise, adjusting the spacing between each node relates to changing

the virtual wavelength of the tubercle. In this way, allowing for optimisation without physical modifications. Just as their hydrodynamic counterpart, they improve aerodynamic performance by increasing lift, reducing drag, and delaying stall. However, performance is sensitive to voltage, with efficiency decreasing above 13kV, and there is a shown potential for closely packed actuators to interfere with each other, which could impact flow control.

2. **Blowing Air**: Al Okbi, Chong and Stalnov [26] demonstrated that leading edge blowing produces an attractive method of active control. The experimental study on a NACA65(12)-10 aerofoil demonstrates that leading edge blowing can effectively mimic and enhance the aerodynamic and even aeroacoustics benefits of serrated leading edges, particularly when the blowing rate is optimised to 10–13% of the main inflow velocity. However, the effectiveness is highly sensitive to blowing parameters and further research is needed to fully understand the underlying flow mechanisms.

Previously, the term “high-lift” was introduced, this typically refers to flaps and/or slats. The earliest documented flap design appeared on the Fairey Hamble Baby in 1916, which employed full-span plain flaps hinged at the trailing edge. This design also integrated ailerons, marking the first use of flaperons. Modern aircraft rely on several flap variants to enhance lift during take-off and landing. Some of these flaps include: Fowler flaps, Gurney flaps, split flaps, and others. Typically, flaps are deflected by about 20° at take-off and up to 40° at landing, when increased drag is beneficial (Anderson, 1991). However, Angelov *et al.* [27] and Abbas *et al.* [28] point out that there is no single established method for determining the optimal gap between the wing’s main element and the flap.

Over the course of this study, attention is directed to slotted trailing edge flaps within a two-element aerofoil configuration, where the fore element serves as the primary aerofoil and the aft element as the flap. The inclusion of a slot eases the requirement for complete pressure recovery at the flap’s trailing edge, a necessity in single-element aerofoils to avoid premature separation. Instead, the fore element can sustain a higher “dumping velocity,” thereby promoting stronger suction and enhanced boundary layer attachment. The aft element then assumes much of the remaining pressure recovery, interacting with the fore element’s wake to maintain favourable flow conditions [29]. Including a detailed account of high-lift systems would exceed the scope of this report; instead, the reader is advised to consult [30] for an extensive guide to the history, theory, and applications of high-lift systems.

Having established the foundational concepts of flow separation, LET and slotted trailing edges, arrival at the primary focus of this investigation has been met: the application of LET to the flap (i.e., the aft element). Although tubercles have been studied extensively on single-element aerofoils, to the best of the author’s knowledge, no documented research has explored their implementation on the aft element leading edge. The only two studies that are available are either employing tubercles on the flap trailing edge [31] or on the fore element leading edge of a two-element aerofoil [32]. This approach is, therefore, believed to be entirely novel. To reflect this novel wavy leading edge on the aft element, the acronym ‘**WALE**’ (Wavy Aft Leading Edge) is defined and used hereafter.

The application of CFD in modelling tubercles has yielded significant insights into their aerodynamic performance across various configurations. For studies involving low Reynolds numbers and tubercles, Tunio *et al.* [33] utilised the RANS approach to model flow behaviour effectively. Hickling and Ingram [34] explored the use of RANS models to analyse the performance of tubercles in transonic S-ducts. Their study highlighted the effectiveness of different turbulence models in predicting flow characteristics and performance measures in transitioning S-duct diffusers. The results indicated that RANS models could provide valuable insights into the flow dynamics associated with tubercles, although the authors noted limitations in capturing transient phenomena. Similarly, Wei *et al.* [35] employed RANS equations to study the impact of leading-edge tubercles on a tapered, swept-back wing at very low Reynolds numbers. Their findings demonstrated that tubercles significantly delayed flow separation and enhanced lift characteristics, confirming the potential of RANS models to accurately predict the aerodynamic benefits of tubercles. This comparison illustrates that, while both studies utilised RANS models, the specific applications and Reynolds number regimes influenced the outcomes and insights gained.

Kim *et al.* [36] investigated the aerodynamic effects of tubercles, showing that they generate complex flow patterns, including counter-rotating vortices that enhance boundary layer momentum exchange. Their findings emphasised the importance of accurate turbulence modelling to capture these effects. Although their study discussed the potential of Large Eddy Simulation (LES) for capturing fine turbulent structures, they reinforced the practicality of RANS models in standard aerodynamic analyses, given the computational resources required for LES. The comparative analysis of various CFD Fluent models for studying tubercles reveals a diverse range of methodologies and findings, and that the specific turbulence model selection significantly influences the accuracy of simulations.

A detailed view of the WALE profile is shown in Figure 9, where C_1, C_2, C_T, A_T denote the first element chord, the second element chord, the modified chord, and the tubercle amplitude. In a conventional two-element aerofoil, the second element chord is constant along the span.

For any given flap angle, β, the total wing chord is $C_W = C_1 + C_2$. Introducing tubercles modifies the flap chord to a sinusoidal function, though its minimum remains C_2:

$$C_T(z) = C_2 + A_T \sin\left(\frac{2\pi}{\lambda} z\right) \quad \textbf{(8)}$$

Hence, the total chord along the span becomes:

$$C_W(z) = C_1 + \left[C_2 + A_T \sin\left(\frac{2\pi}{\lambda} z\right)\right] \cos(\beta) \qquad 0 \le z \le b \quad \textbf{(9)}$$

The peak and trough positions along the span are defined by the function:

$$\mathcal{U}(z) = 12.7n \begin{cases} \text{Max} & \text{if } n \text{ is odd} \\ \text{Min} & \text{if } n \text{ is even} \end{cases} \quad \textbf{(10)}$$

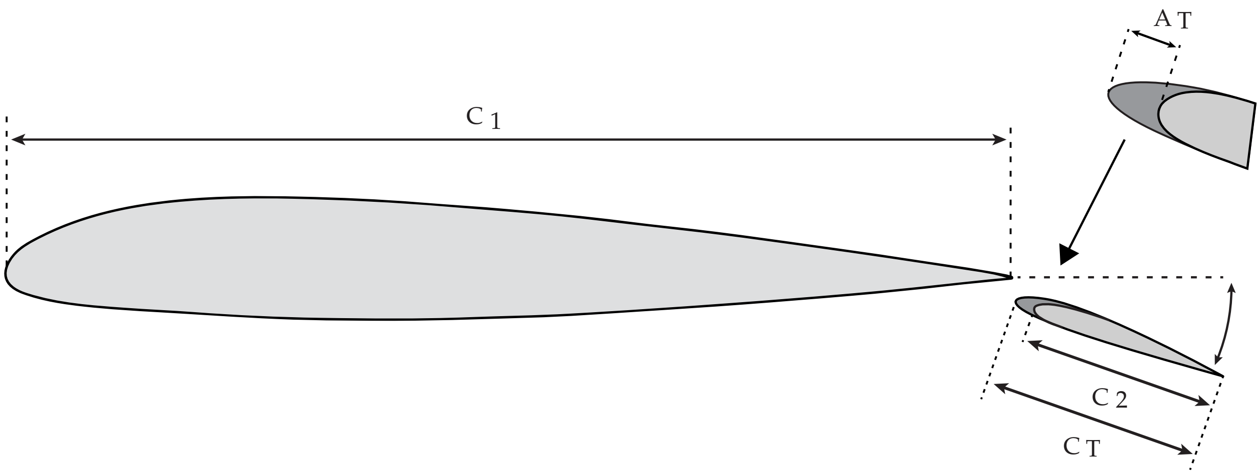

Fig. 9. Profile view of NACA 23012 with modified LET flap

5. METHODOLOGY

The present study uses CFD to explore the effects of introducing a wavy flap leading edge. Ideally, wind tunnel experiments would also have been conducted, as they provide direct and robust validation data for pressure distributions, lift, and drag characteristics at various angles of attack. CFD methods, employing Reynolds-averaged Navier-Stokes (RANS) turbulence models are most valuable when supplemented and validated by such experimental data. However, wind tunnel testing was not feasible in this research because the subsonic wind tunnels currently available at Brunel University lack the scale, accuracy, and operational flexibility required for any meaningful analysis of the modified aerofoil-flap system studied here. This limitation called for a reliance on CFD and placed constraints on the scope of validation possible, to mitigate this constraint, considerable effort was made to leverage the validation data available in the literature- albeit limited for aerofoils featuring flaps. It is useful to recall the statement by the statistician George P. E. Box, "*Remember that all models are wrong; the practical question is how wrong do they have to be to not be useful.*" This perspective, though for statistical analysis, pertains well to CFD. Without validation and verification, all CFD models comprise of inherent simplifications and assumptions, nothing more. It is thus crucial to evaluate the extent of these limitations and ensure the selected models provide results that remain practically meaningful and reliable within the context of aerodynamic analysis, this evaluation is done by mesh convergence and validation tests, it is only after these test that standards can be made. In the following sections, a brief contextual overview of the turbulence modelling choice is first provided, followed by a detailed description of the modified aerofoil geometry. Subsequently, the chosen meshing strategy is outlined.

A. Turbulence Modelling

Incompressible turbulent flow around an aerofoil is governed by the Navier-Stokes and continuity equations. However, directly solving these Partial Differential Equations is impractical for real-world applications due to the computational intensity of capturing turbulent fluctuations. Consequently, the Reynolds-Averaged Navier-Stokes (RANS) equations were utilised, allowing for a feasible approximation of the turbulent behaviour through time- averaged terms. The derivation of the RANS equations introduces averaged momentum equations from the Navier-Stokes equations, leading to additional terms representing the turbulent stress which require turbulence modelling to resolve the effects of these fluctuations. Full numerical solutions of the Navier Stoke's Equations take over a century for full body solutions. For general use, turbulence models have been developed.

The flow simulation employed the RANS method and more specifically, the k–ω SST model to solve for turbulent viscosity. This model combines the accuracy of the k–ω model in the boundary layer region with the good agreement that the k–ε model shows in the freestream.

To have a transport equation for the turbulence variables, the RANS equation is multiplied by the function $(1 - F_1)$ in Eq. (11):

$$\frac{\partial(\rho\varepsilon)}{\partial t} + \frac{\partial(\rho U_i \varepsilon)}{\partial x_i} = \frac{\partial}{\partial x_j}\left[\left(\mu + \frac{\mu_t}{\sigma_\varepsilon}\right)\frac{\partial \varepsilon}{\partial x_j}\right] + \frac{\gamma}{\nu_t}P_k - \beta\rho\omega^2 + (1 - F_1)\frac{2\rho\sigma_\omega^2}{\omega}\Delta k \cdot \Delta\omega \quad (11)$$

The value for F_1 depends on the proximity of the cell to the wall and dictates which turbulent model to use and so it is called the Blending function which is used for a smooth transition between k–ω model and the k–ε model.

Turbulent viscosity for the *SST* model is found using Eq. (12):

$$\mu_t = \frac{a_1 \rho k}{\max(a_1\omega, SF_2)} \quad (12)$$

Where F_2 is another blending function and S is *[shear strain]*. Figure 10 is given to illustrate how the Blending function varies with proximity to a wall. Alternative RANS turbulence models were considered but not selected. The k–ε model, while widely used due to its simplicity and efficiency, shows limitations under strong adverse pressure gradients, separation, and curvature. Conversely, the standard k–ω model offers superior near-wall accuracy and improved numerical performance in adverse-pressure-gradient flows but remains notably sensitive to free-stream turbulence conditions. This sensitivity can lead to inaccuracies in predicting separated flow regions. Therefore, the SST approach was deliberately selected to balance these considerations.

B. Validation and Geometry

This next section provides a comprehensive examination of the methodology for modeling flow over a two-element aerofoil with leading-edge tubercles on the aft element. The study is began by a validation case. Afterwards the model of the aerofoil is created and then key dimensions are set for it.

B.1. Validation (0.508m x 0.508m)

The purpose of validation is to ensure results are independent of the mesh, and they are indeed reliable. This section first discusses the validations setup, then going into the Mesh Independence study and finally it concludes with the Validation results. The initial approach mirrors the structure of previous engineering literature. The Validation leverages NACA Report 614 [37], giving experimental data for a NACA 23012 with a plain flap, tested in the variable-density wind tunnel at Langley. Carried out in the N.A.C.A. 7 by 10 foot open-jet wind tunnel, a sufficiently large test section as this is used to minimise wall-boundary effects and approximate two-dimensional flow around the model. To eliminate spanwise flow mostly due to tip-effects, large circular end plates on the model were mounted.

The aerofoil tested was a N.A.C.A. 23012 profile with a span and chord of 508 mm. Attached to this was an external-aerofoil flap, also a N.A.C.A. 23012 aerofoil. The flap spanned the same 508 mm but was scaled down to 20% of the main chord. A hinge axis on the flap allowed deflections from $-10°$ to $+60°$; For this current report, the flap angle $20°$ will be used.

All experiments were conducted at a nominal air speed of 80 mph under standard sea-level conditions, Re (based on combined chord of aerofoil plus flap) is given as 1,460,000 however to account for the wind-tunnel turbulence factor of 1, an effective Reynolds number of about 2,040,000 was used in analysis. To capture pressure distributions, a series of pressure orifices were placed along the chord lines of both the main aerofoil and the flap, special attention is given to the aft leading edge, ensuring a greater density of orifices are placed to capture complex flow . The recorded pressures were then converted to dimensionless pressure coefficients $\left(\frac{p}{q_\infty}\right)$ and used to construct pressure diagrams and surface integrals were performed to determine lift characteristic.

A structured C-mesh approach proved difficult for the slotted aerofoil, owing to geometric complexity around the flap gap. Maintaining low skewness and acceptable aspect ratios sub 1000 across the flap interface would require either excessive cell counts or high cell distortion. Consequently, a rectangular domain was assembled around the slotted aerofoil, extending 35 chord lengths in the x-direction and 20 chord lengths in the y-direction. Within this domain, T-Rex (*anisotropic tetrahedral extrusion*) was used to generate high-quality boundary-layer cells normal to the aerofoil and flap surfaces. This method ensures a near-wall spacing that achieves $y^+ = 1$, resolving the viscous sublayer adequately. First cell height of 0.000098 and 0.000064 is used for the main aerofoil and flap respectively, with growth rate of 1.15. Away from the boundary layer, the grid transitions to coarser unstructured cells, balancing computational cost with accuracy.

A mesh-independence investigation was conducted using the slotted aerofoil configuration. The number of connectors in the computational domain was increased systematically, approximately by a factor of 1.5 at each refinement step, doing so, several successively refined domains were generated, ranging from approximately 13,000 cells up to 90,000 cells (in 2D). Figure 10 (below) illustrate sample lift values (in Newtons) for different mesh densities. As the mesh resolution increases beyond roughly 50,000 cells, the lift stabilises around 466 N, demonstrating that further refinement yields diminishing returns.

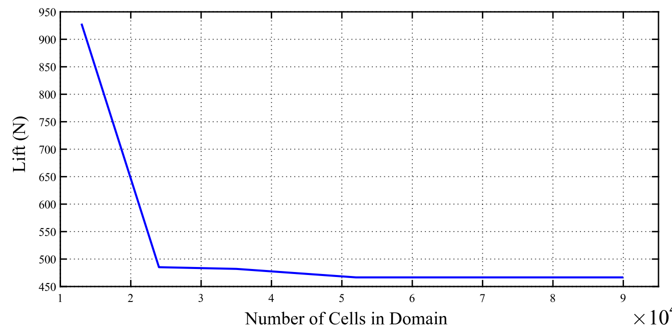

Fig. 10. Mesh Independence Study for the Slotted Aerofoil. Plot of lift (N) versus number of cells, showing convergence at around 50 000 cells.

The validation study employed the k–ω–SST turbulence model to investigate the aerodynamic performance of the aerofoil at various angles of attack. The CFD simulations were conducted using an initial inlet velocity ($U = 35.8\ \mathrm{ms}^{-1}, V = 0\ \mathrm{ms}^{-1}$), with subsequent parametric variations of velocity components corresponding to changes in angle. The SIMPLE algorithm was employed as the solution method. Figure 11 shows clearly the variation of C_L with increasing angles of attack. Both the CFD results and the validation data from Wenzinger demonstrate a similar trend, with lift coefficient values rising steadily until a plateau is reached, signifying a decrease in lift slope at higher angles.

This plateau indicates the onset of flow separation over the aerofoil surface, where further increases in angle of attack result in reduced lift increment and eventually, stall conditions. The validation data from Wenzinger (1938) is limited to angles between $0°$ and $9.3°$, yet within this range, the trend closely aligns with the CFD results. It can be noticed that between $8°$ and $9°$, the line begins to flatten, suggesting that flow is beginning to reverse and separate. To see whether this is true, the CFD results have been extended beyond this range (up to $16°$), confirming the expected post-stall decrease in lift.

A comparison between the CFD and experimental validation lift values is summarised in Table 1. The percentage differences for all angles of attack remain well below 5%, indicating strong agreement and validating the accuracy of the numerical model. A slightly higher difference (4.55%) occurs at the $9.3°$ angle; this is most likely due to the model's difficulty in resolving the flow separation accurately at this critical angle. Numerical predictions become more challenging at higher angles of attack that approach stall conditions, as turbulent and separated flow regions become increasingly complex. These complex flow phenomena often lead to increased sensitivity in turbulence modelling within boundary layer treatment.

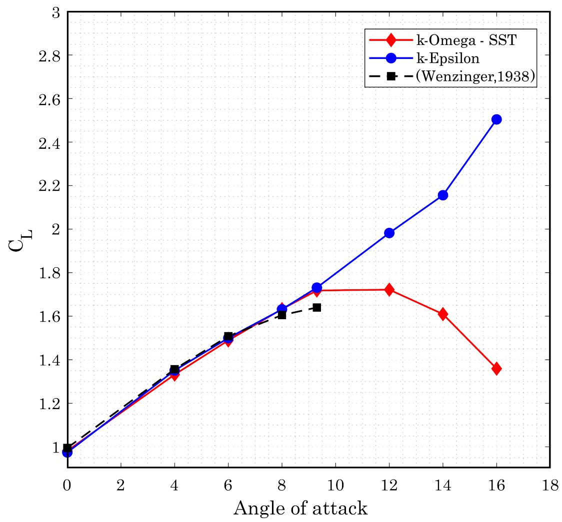

Fig. 11. Comparison of C_L versus angle of attack between CFD results (k–ω SST model and Standard k–ε) and experimental data [37].

Table 1. Comparison between k–ω SST and [37] lift values

Angle(°)	CFD Lift (N)	[37] (N)	Δ%
0	476.46	470.00	1.37
4	649.64	637.80	1.86
6	722.27	712.89	1.32
8	768.56	781.80	1.69
9.3	785.32	822.74	4.55

Despite this discrepancy, the overall trend remains consistent. The k–ε model has been plotted to compliment the k–ω–SST model, unsurprisingly it is superior over the k–ω–SST model pre-stall. It is known that its strengths lie in resolving flows in the freestream; it, however, completely fails to predict stall and even acknowledge it. This model is not known for resolving complex flows and geometries, its focus being on internal and industrial flows rather than aero applications. In conclusion, the CFD results obtained using the k–ω–SST model and SIMPLE algorithm demonstrate suitable agreement with established experimental data, thus the validation

B.2. WALE Geometry

For the modified case, SolidWorks 2025 was used for geometry construction. Initially, the NACA 23012 aerofoil profile coordinates from AerofoilTools were imported to create a curve through *xyz* points. Two changes have been made, first, the original intended span of 508 mm was reduced to a span of 105 mm, to save computational power, and second, the operating velocity is increased to $50\,\mathrm{ms}^{-1}$ to ensure Reynold's number is in the 10^6 range. The geometry features six tubercle bumps with a wavelength (λ) of 0.021 m and amplitude (A_T) of 0.01 m. Offset planes were created at intervals of $\frac{1}{4}\lambda$. Two distinct profiles were generated: the original NACA 23012 baseline flap profile and a second profile duplicated from the baseline flap and scaled up (+) using the formula,

$$ScaleFactor = 1 \pm \frac{A_T}{C_2},$$

with the trailing edge corner point as the scaling centre.

These two distinct profiles were then repeatedly offset and a loft operation was performed through all of them to create the final geometry (Figure 12). This method is taken from [38].

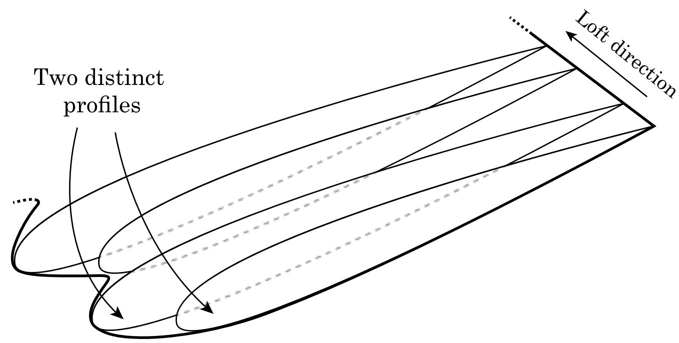

Fig. 12. Diagram of two seperate profiles used to create geometry, loft direction specificed in the direction of the arrow.

The mesh generation was as follows. First, the CAD STEP file containing the main aerofoil and the WALE flap geometry was imported into Pointwise Fidelity. Upon import, connectors were defined along the upper and lower surfaces of each aerofoil body. Each connector was set to contain 200 points with a spacing of 0.1 at the leading and trailing edges, ensuring suitable resolution. Surface domains were then created on the main and wavy aerofoils, and the *Grid* → *Solve* tool was used to refine the wavy flap domain based on surface curvature settings. A surface deviation value of 1.1×10^{-5} and an angle limit of 15° was used, iterated as necessary until the domain conformed accurately to the curved geometry. Afterwards, rectangular outer boundary was constructed, spanning 10 chord lengths above and below the aerofoil and extending 20 chord lengths downstream. Connectors for this boundary were dimensioned 160 by 100. The rectangular domain was subsequently duplicated and translated by the chosen span (0.105 m) establishing the three-dimensional extent of the flow field. To accommodate symmetry boundaries and maintain appropriate face orientation, *Assemble Special* → *Domain* was utilised, aligning the rectangle boundaries opposite the aerofoil profile. With all outer boundaries defined, a block was assembled by selecting the rectangle domain faces and attaching them to the adjacent aerofoil surfaces. After forming the block, initial tetrahedral elements were generated, followed by setting up T-Rex boundary-layer meshing. Number of layers was set to 40 and in the Advanced tab, anisotropic seeding was set to 1.0. After selecting the wing surface as a Wall boundary condition with initial cell height as 1.1×10^{-5}, the smoothing phase began to reduce cells with a maximum included angle greater than 175°, through multiple iterations of *Grid* → *Solve* → *Attributes*, the target included angle threshold was lowered stepwise – beginning at 175°, then 170°, and finally 155° – while re-running the smoothing process until the desired mesh quality criteria were satisfied.

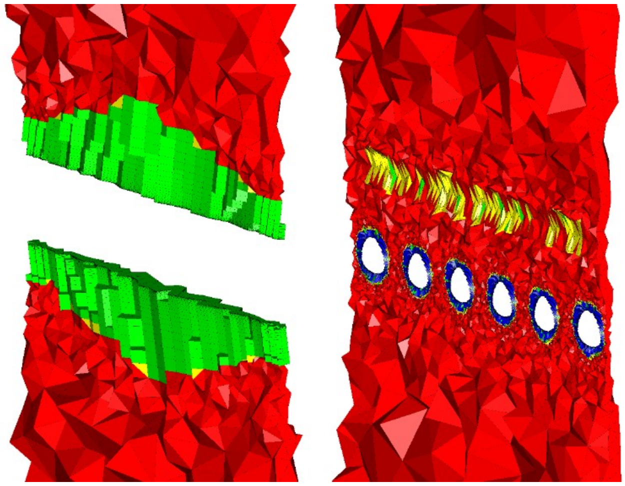

Fig. 13. A vertical y-axis cut shows the aerofoil's boundary layer growing from fine near-wall cells to a coarser outer mesh, while a second cut reveals the refined cell structure around the tubercle peaks, capturing essential curvature and flow details

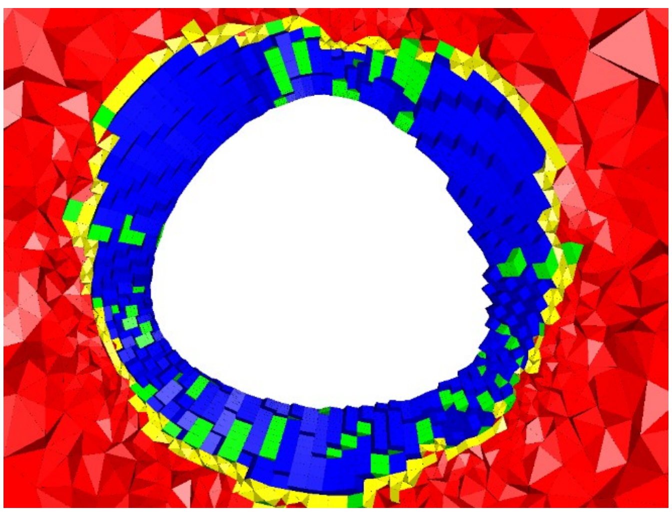

Fig. 14. A close-up view of the mesh cut around tubercle peak, clearly showing a transition from coarse triangular elements (in red) to more refined rectangular blocks (in blue and green). The yellow zone indicates an intermediate interface that helps maintain a smooth progression in cell size.

6. RESULTS AND ANALYSIS

Figure 15 presents the isosurface of Q–criterion at 175 000 for the modified flap with tubercles at a 0 angle of attack. Several distinct features stand out. First, each trough region generates a prominent, streamwise vortex visible as a "corkscrew" structure in the iso-surface plot, as the flow reaches the trailing edge of the flap this structure appears to become a large horseshoe vortex, in which its apex has risen into high pressure regions, suggesting that the vortices formed by the bumps are sensitive structures. This may be due to the extra pressure that is dumped onto the flap by the fore element of the aerofoil. In spite of this, these coherent structures confirm that tubercles can create organised streamwise vortex pairs, particularly in the trough regions. It can also be seen that the pressure at the start of the trough is significantly higher, because the geometry forces the flow to decelerate and partially stagnate, causing a local pressure rise. By comparing this flow pattern to that described in existing literature [39], it is apparent that the sinusoidal leading edge forces the flow to roll up where the local chord is effectively shortened, when $\mathcal{V}(z = n_{\text{odd}})$.

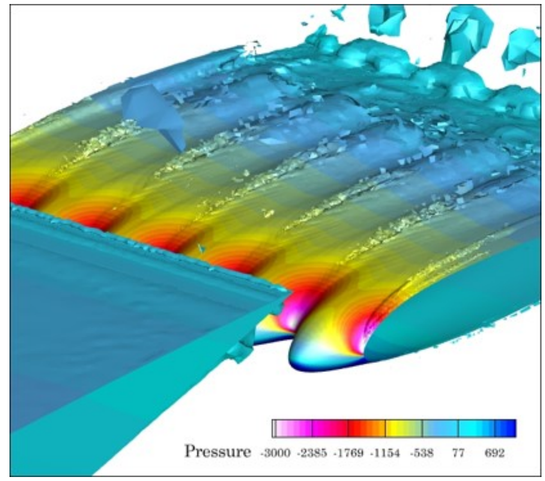

Fig. 15. 0 degrees Isosurface of Q–criterion onto WALE flap, at q value of 170,000

Figure 17 shows a velocity streamline plot facing the leading edge bump, at $\left(\frac{x}{c_z} = 0.08\right)$, illustrating the presence of vortices forming at the tubercle peaks and how the vortices at a peak location evolve across three key angles of attack (8°, 14°, and 16°). At lower angles (e.g. 8°), the vortex core remains compact, and the surrounding flow lines wrap tightly around it, comparing this with higher angles, the strength of the vortex is weaker. As the angle of attack increases to 14°, the vortex grows stronger, reflecting the higher adverse pressure gradient that drives the swirl. Once the wing approaches the stall angle (here near 16°), the vortex begins to break down, and portions of its swirling structure 'leak' into adjacent flow regions. This breakdown reduces the coherence of the vortex core, signalling an imminent or partial loss of the aerodynamic benefits it was providing (such as energising the boundary layer). Between 8° and 14°, the vortex core diameter increases from 0.004527 m to 0.007214 m, a gain of 0.002687 m over 6°. Treating this range as representative of a linear trend in the pre-stall regime yields an estimated growth rate of approximately 4.48×10^{-4} m per degree. This means that each additional degree of angle of attack in this regime appears to enlarge the vortex core diameter by roughly 0.00045 m.

Overall, the sequence demonstrates partial agreement with previous findings [40] that vortical flow often begins along blunter edges at higher angles of attack, however in this case it is the strength of vortical flow that increases with angle. The following diagram in Figure 17 illustrates what is theorised to be happening on the flap's upper surface. As the oncoming flow encounters the peaks, it generates the weaker "Peak Vortices" shown in red, acting as a partial barrier, a 'Virtual Wall', that initially seals off the trough from the main flow. Meanwhile, flow accelerates into the trough due to the curvature and the Coanda effect, which forces the fluid that does enter to speed up and swirl more vigorously inside the trough region, this would

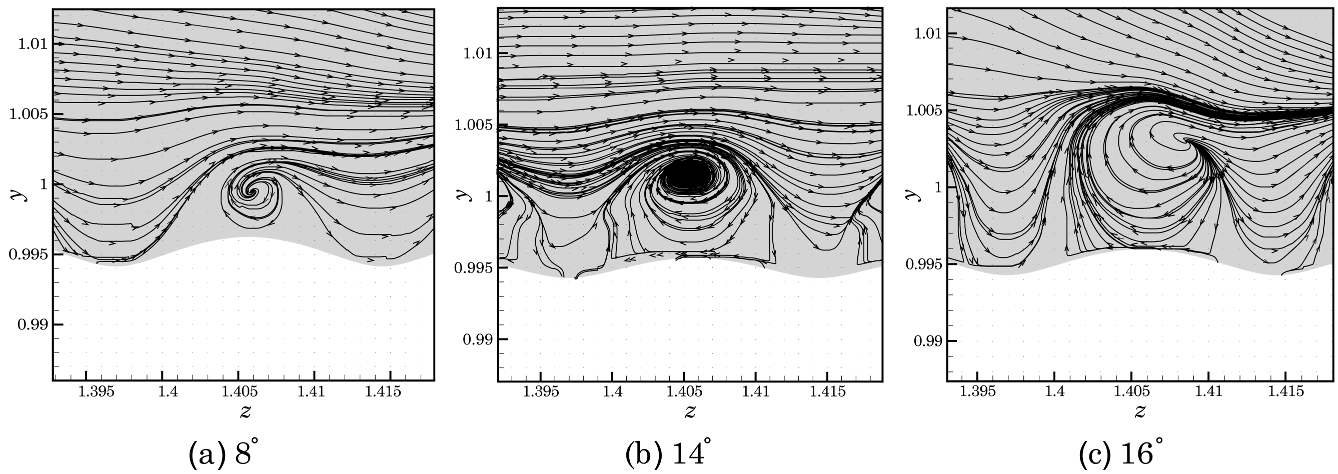

Fig. 16. Velocity streamline plot at $x/c_z = 0.08$ across tubercle peaks at 8°, 14°, and 16° angles of attack

explain the high strain rate regions in Figure 15. Over time, these two sets of vortices will evolve and may merge especially as angles of attack increase and local pressure changes promote vortex breakdown or leakage. All plots previously presented in this section confirm that tubercle peaks and troughs still create coherent vortices on the flap, thus meeting Objective 1. The remainder of this section is devoted to analysing Objective 2, specifically whether the flap tubercles effectively delay stall and enhance lift.

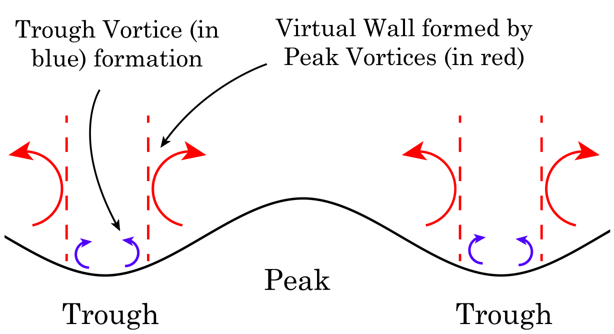

Fig. 17. Velocity streamline plot at $x/c_z = 0.08$ across tubercle peaks at 8°, 14°, and 16° angles of attack.

In Figure 18 (a), the WALE configuration consistently generates higher lift than the baseline across the entire range of angles of attack, except at 0°–7°, where the curves are nearly identical. From 7° onwards, the difference becomes increasingly noticeable. The most significant region of divergence occurs from 10° to 16°, where the WALE configuration maintains consistently higher lift. For example, at 16°, the WALE achieves a maximum lift coefficient of approximately 2.1 compared to the baseline's 1.8, an increase of about 23%. The baseline peaks earlier at 14° with a lower value of $C_{L,\max}$. The increase in stall angle is 12.5%. This increase in lift may be due to the high suction zones that form near the troughs which may contribute to more lift by increasing the overall pressure differential across the flap. After 14°, the baseline experiences a sharp decline in lift indicating abrupt stall. In contrast, the WALE shows only a mild reduction in lift between 14° and 16°-the rate of lift loss is 0.1 per degree, which is much more gradual compared to the 0.5 per degree seen in the baseline. This reflects a softer, more controlled stall in the WALE, likely due to streamwise vortices enhancing boundary layer attachment.

In Figure 18 (b), the pitching moment trend reveals a distinct difference in stability characteristics. The WALE configuration shows a steadily increasing moment with a noticeably steeper gradient from 4° to 14°, peaking around 0.13 at 14°, whereas the baseline maintains a flatter, more stable curve, peaking lower at around 0.08. The rate at which the WALE configuration drops after stall is slightly lower than the baseline, supporting that stall is more controlled for the former. However, the steeper positive gradient of the WALE curve from 4° to 14° suggests reduced static longitudinal stability. Note that a more stable aerofoil would exhibit a lower pitching moment slope, indicating less sensitivity to angle of attack changes. In contrast, the WALE aerofoil has a higher slope which implies that small changes in angle produce more significant shifts in pitching tendency. The reduced stability in the WALE configuration can be attributed to the geometry, which introduces strong three-dimensional flow structures that, while beneficial for lift, cause a less uniform pressure distribution. Potentially, this could make the centre of pressure more sensitive to angle change.

Additionally, the interaction between the fore element's wake and the flap may become more complex when paired with tubercles, especially as angle of attack increases, it is not clear as of now why. Another possible cause of the reduced stability in the WALE wing is that vortex breakdown over the WALE flap could occur unevenly across the span, introducing further instability. All plots presented here confirm that tubercle peaks and troughs

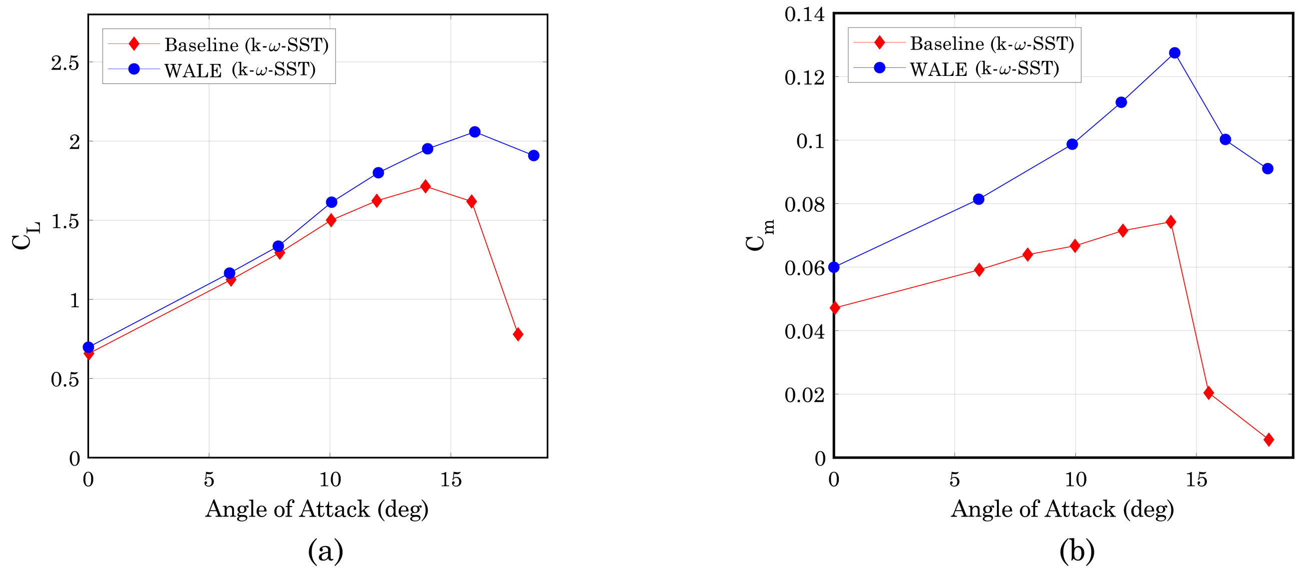

Fig. 18. Comparison of (a) Lift Coefficient (C_L) and (b) Moment Coefficient (C_m).

generate coherent vortices on the flap, meeting Objective 2. The next step involves a more careful examination of the post-stall behaviour of both aerofoils, a spanwise-averaged lift coefficient is taken by slicing the WALE flap into 40 planes in Tecplot 360, integrating the pressure to obtain 40 averaged pressure points along the flap chord, and multiplying each averaged pressure value by aerofoil chord to obtain Lift. In Figure 20, the blue curve stays noticeably higher than the baseline through much of the mid-chord range, culminating in a plateau from 0.18 to 0.7 normalised flap chord, this clearly indicates more sustained lift compared to the earlier drop in the baseline line which strongly suggests that tubercles on the leading edge of a flap delay stall by inducing vortices that energise the boundary layer, keeping the flow attached for longer. As a result, WALE maintains a higher loading level over the flap chord, whereas the baseline begins to lose lift earlier.

The baseline has a greater lift at flap chord = 0, this is most likely because the tubercles lift distribution spanwise is not constant, meaning there are components of lift (most on the peaks) that are below 0. This is however a small drawback to the WALE arrangement, and does not take away from the benefits it has so far brought. Figure **??** compares surface sheer stress streamlines on the baseline and WALE flaps at a post-stall angle of 18°. In the baseline case, an obvious separation bubble appears early along the chord, followed by a pronounced trailing-edge separation line that extends across spanwise. By contrast, the WALE flap reveals substantially more attached flow, especially near the peak regions. Although small, discrete vortices form downstream at each trough, their influence seems to be relatively contained, and separation on a large scale is avoided. This visual evidence serves to reinforce the idea that tubercle peaks and troughs channel the flow more effectively, helping the WALE flap sustain attached flow in post-stall flow regimes.

It is important to note that all scientific research, at all levels,

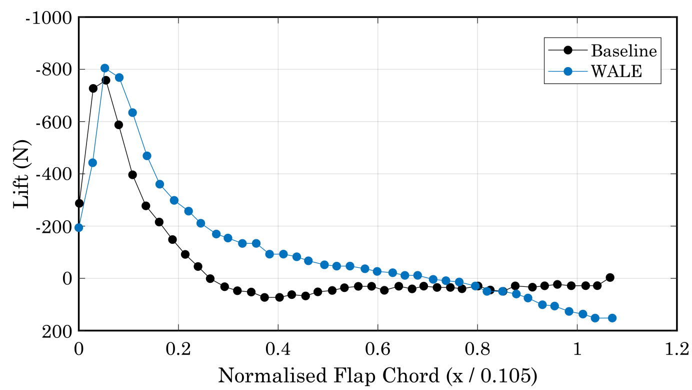

Fig. 19. Spanwise lift variation with flap chord.

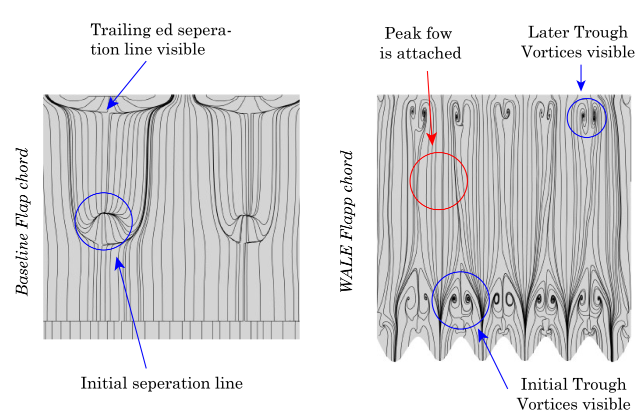

Fig. 20. Surface shear stress visualised for both flaps tested.

suffers limitation, it is the extent to which these limitations are addressed which distinguishes good research. Three principal constraints have been recognised that may affect the quality of the findings.

Firstly, there is an issue of lack of prior work on tubercles for flaps-only two studies have been to address anything similar. Consequently, the present analysis has relied heavily on single-element tubercle data, and the flow characteristics around them. This means that potential techniques or flow characteristics have not been explored to its full potential. Second, no direct wind tunnel data were obtained for the primary case study, while numerical limitation was performed, with suitable mesh size and validation confirmed. The k–ω SST turbulence model, although robust and well-suited for separated flows, inevitably approximates unsteady turbulent structures, especially in regions of strong curvature near the flap leading edge. This means that transient vortex breakdown or any small-scale flow structures might not be captured with full fidelity. Lastly, the experimental dataset used for validation dates to NASA's 1938 experiments on a 23012 aerofoil. Reliance on any data nearly a century old entails potential discrepancies in measurement protocol and result validation. Certain specifics of the setup such as tunnel corrections could not be replicated in CFD. Still, the report was chosen due to its rigorous procedures along with the well-characterised NACA 23012 geometry, this provided a strong basis for comparison.

7. CONCLUSIONS

A. Conclusions from the Investigation

This study set out to determine the effects of tubercles on the leading edge of aft elements in multi-element aerofoils, with two objectives: (1) Whether tubercles on a slotted flap (WALE) can maintain streamwise vortices under the influence of the main element's wake, and (2) Whether those vortices delay stall and improve overall lift. Numerical evidence from spanwise velocity streamlines and surface sheer stress streamlines show that tubercles indeed generate discrete vortex structures over a range of angles of attack, thereby fulfilling the first objective. The purpose of these vortices is apparent, to sustain attached flow.

In the comparing of WALE and baseline configurations, the WALE flap not only exhibited a higher $C_{L,\max}$, but also experienced a more gradual drop in lift post-stall, this is in line with theory. This behaviour is attributed to boundary layer energisation due to tubercles, in the same sense how VG's allow for delay of flow separation. Although this design boosts lift, it was found that the introduction of tubercles introduces an pre-stall steeper pitching moment gradient, reflecting increased sensitivity to changes in angle. This can possibly be explained by the increased number of streamwise vortices over the flap surface, interacting with the fore element's wake, however it is not completely known why this different in $\frac{dC_M}{d\alpha}$ is seen. Overall, the original aim and objectives of this investigation have thus been met.

B. Suggestions for Further Work

Future work would benefit from wind tunnel experiments on a scaled, instrumented flap model, allowing direct measurement of surface forces and pressure distributions, and flow visualisation to confirm CFD-based observations. Parametric studies of flap tubercle amplitude, wavelength, and phase could create more optimal patterns for different flight regimes, this would also be very beneficial in exploring in future studies. In parallel with wind-tunnel experiments, hybrid CFD methods such as DES could shed greater light on unsteady vortex interactions with the main elements wake. Exploring how the geometry performs under dynamic flap deflections and within an integrated high-lift system (including a sleave which contains the WALE flap when unused) would be able to clarify the full effects of tubercles in a mechanically integrated setting.

REFERENCES

1. The Royal Society, "Net zero aviation fuels: resource requirements and environmental impacts. policy briefing," https://royalsociety.org/-/media/policy/projects/net-zero-aviation/net-zero-aviation-fuels-policy-briefing.pdf (n.d.). [online].
2. R. Bryant, "Research tutorial on thermoplastic composite technology," https://ntrs.nasa.gov/citations/20205006952 (2020). [online; accessed 11 February 2025].
3. J. Jiménez, "Coherent structures in wall-bounded turbulence," J. Fluid Mech. **842** (2018).
4. P. Baines, S. Majumdar, and H. Mitsudera, "The mechanics of the tollmien–schlichting wave," J. Fluid Mech. **312**, 107–124 (1996).
5. H. Lomax, T. Pulliam, and D. Zingg, *Fundamentals of Computational Fluid Dynamics* (Springer Science & Business Media, 2013).
6. Micro AeroDynamics Inc, "How micro vortex generators work?" https://microaero.com/how-micro-vortex-generators-work/ (2023). [online; accessed 28 January 2025].
7. B. Bhushan, "Biomimetics: lessons from nature–an overview," Philos. Trans. Royal Soc. A: Math. Phys. Eng. Sci. **367**, 1445–1486 (2009).
8. M. Özden, M. S. Genç, and K. Koca, "Investigation of the effect of hidden vortex generator–flap integrated mechanism revealed in low velocities on wind turbine blade flow," Energy Convers. Manag. **287**, 117107 (2023).
9. A. Andrew, "Hidden vortex generators," https://patents.google.com/patent/US4039161A/en (1975). [online; accessed 21 December 2024].
10. B. Fox and S. Fox, "Retractable vortex generator for reducing stall speed," https://patents.google.com/patent/US20130009016A1/en (2014).
11. J. Narramore, "Retractable vortex generator," https://patents.google.com/patent/EP1896323B1/en (2009).
12. F. Fish and J. Battle, "Hydrodynamic design of the humpback whale flipper," J. Morphol. **225**, 51–60 (1995).
13. V. Walters, "Body form and swimming performance in the scombroid fishes," Am. Zoöl. **2**, 143–149 (1962).
14. D. Bushnell, "Drag reduction in nature," Annu. Rev. Fluid Mech. **23**, 65–79 (1991).
15. F. Fish, P. Weber, M. Murray, and L. Howle, "The tubercles on humpback whales' flippers: application of bio-inspired technology," Integr. Comp. Biol. **51**, 203–213 (2011).
16. P. Watts and F. Fish, "The influence of passive, leading edge tubercles on wing performance," https://www.otherpower.com/images/scimages/2637/leading_edge_tubercles.pdf (2001). [online].
17. D. Miklosovic, M. Murray, L. Howle, and F. Fish, "Leading-edge tubercles delay stall on humpback whale (megaptera novaeangliae) flippers," Phys. Fluids **16**, L39–L42 (2004).
18. X. Zhang, C. Zhou, T. Zhang, and J. Wen-ying, "Numerical study on effect of leading-edge tubercles," Aircr. Eng. Aerosp. Technol. **85**, 247–257 (2013).
19. M. Keerthi, M. Rajeshwaran, A. Kushari, and A. De, "Effect of leading-edge tubercles on compressor cascade performance," AIAA J. **54**, 912–923 (2016).
20. B. Stein and M. Murray, "Stall mechanism analysis of humpback whale

flipper models," in *Proceedings of Unmanned Untethered Submersible Technology (UUST),* (Durham, 2005), p. 5.
21. J. Joseph and A. Sathyabhama, "Experimental study on the effect of tubercle on aerodynamic characteristics of swept wings at low reynolds number," Iran. J. Sci. Technol. Trans. Mech. Eng. **46**, 783–792 (2021).
22. J. Joseph, A. Sathyabhama, and S. Sridhar, "Experimental and numerical analysis of humpback whale inspired tubercles on swept wings," Aircr. Eng. Aerosp. Technol. (2022).
23. A. Sidorenko, A. Budovskiy, A. Maslov, *et al.*, "Plasma control of vortex flow on a delta wing at high angles of attack," Exp. Fluids **54** (2013).
24. H. Pedro and M. Kobayashi, "Numerical study of stall delay on humpback whale flippers," https://www.hawaii.edu/hpc/pedro_paper.pdf (2008). [online; accessed 16 February 2025].
25. A. Abbasi, X. Meng, and H. Li, "Effects of wavelength and amplitude variation on the plasma leading edge tubercles," in *Proceedings of the IEEE International Conference on Bio-inspired Computing (IBCAST),* (2019), pp. 816–823.
26. Y. Al-Okbi, T. Chong, and O. Stalnov, "Leading edge blowing to mimic and enhance the serration effects for aerofoil," Appl. Sci. **11**, 2593 (2021).
27. I. Angelov and C. Velkova, "Influence of a slotted flap gap size on the aerodynamic characteristics of a light aircraft wing at taking off and landing," in *2020 IEEE European Conference on Electrical Engineering and Applications,* (2020).
28. A. Abbas, A. Khudheyer, and J. Hussain, "Investigation the effect of flap design optimization on wake propagation behind wings of transport plan," ARPN J. Eng. Appl. Sci. **13**, 8393 (2018).
29. A. Smith, "High-lift aerodynamics," J. Aircr. (1975). [online].
30. J. Wild, *High-lift aerodynamics* (CRC Press, 2022), 1st ed.
31. A. Knepper, "Examination of three candidate technologies for high-lift devices on an aircraft wing," Tech. rep., – (2005). [online].
32. R. Mehta, R. Perez, and P. Jansen, "Aerodynamic characteristics of tubercled slotted flaps," in *AIAA Aviation 2019 Forum,* (2019).
33. I. Tunio, T. Hussain, I. N. Unar, *et al.*, "Turbulence model study for aerodynamic analysis of tubercle leading edge wing for low reynolds number flows," https://www.researchgate.net/publication/381157389_Turbulence_model_study_for_aerodynamic_analysis_of_tubercle_leading_edge_wing_for_low_Reynolds_number_flows (2024). [online].
34. T. Hickling and G. Ingram, "Reynolds-averaged navier–stokes modelling in transonic s-ducts with passive flow control," Proc. Inst. Mech. Eng. Part A: J. Power Energy **234**, 31–45 (2019).
35. Z. Wei, T. New, and Y. Cui, "Aerodynamic performance and surface flow structures of leading-edge tubercled tapered swept-back wings," AIAA J. **56**, 423–431 (2018).
36. H. Kim, J. Kim, and H. Choi, "Flow structure modifications by leading-edge tubercles on a 3d wing," Bioinspiration & Biomimetics **13**, 066011 (2018).
37. C. Wenzinger, "Pressure distribution over an naca 23012 airfoil with an naca 23012 external-airfoil flap," Tech. rep., NTRS (NASA Technical Reports Server) (1938). [online].
38. Learning Mentor, "How to create an airfoil with tubercles in solidworks," https://www.youtube.com/watch?v=h8a9HUGpzuE (2022). [online; accessed 6 March 2025].
39. M. Zhao, M. Zhang, and J. Xu, "Flow physics behind the effects of leading-edge protuberances on the airfoil aerodynamic performance," J. Physics: Conf. Ser. **1037**, 022035 (2018).
40. J. Luckring, "A survey of factors affecting blunt leading-edge separation for swept and semi-slender wings," in *28th AIAA Applied Aerodynamics Conference,* (Chicago, 2010).